Influence of microstructure on the erosive wear behaviour of Ca α-sialon materials

Y. Zhang [a,*], Y.-B. Cheng [a], S. Lathabai [b]

[a]*Department of Materials Engineering, Monash University, Victoria 3800, Australia*
[b]*CSIRO Manufacturing Science and Technology, Woodville, South Australia 5011, Australia*

Abstract

The erosion behaviour of three pressureless sintered Ca α-sialon ceramics with different grain sizes, morphologies and various amounts of grain boundary glass was investigated using a gas-blast type erosion rig. The erodent particles used were SiC grits. The effects of grain size and morphology on the erosion mechanism were studied. It was found that the dominant material removal mechanism for the fine equiaxed-grained sialon was grain dislodgment, while that for the elongate-grained material was transgranular fracture. The effect of different amounts of intergranular glass on the erosion resistance of these materials was also studied. It was found that an optimum amount of grain boundary glass had a beneficial effect on erosion resistance. Finally, the effect of post-sintering heat treatment on the erosion behaviour of these materials was investigated. The results showed that heat-treated samples exhibited a higher erosion rate than their as-sintered counterparts. © 2001 Elsevier Science Ltd. All rights reserved.

Keywords: Erosive wear; Grain boundaries; Microstructure-final; Sialon; Wear resistance

1. Introduction

Compared to most brittle materials, sialon ceramics exhibit excellent erosion resistance.[1,2] There are two crystallographic modifications of sialon, α and β. α-Sialons have, in general, an equiaxed grain morphology and high hardness,[3] while β-sialons tend to form elongated grains and exhibit significantly higher toughness and lower hardness than α-sialons.[4] α/β-Sialon composites offer some improved mechanical properties due to the combination of the high hardness of the α-sialon phase and the strength and toughness of the elongated β-sialon grains. In particular, it has been shown that α/β-sialon composites possess an order of magnitude greater erosion resistance than β-Si$_3$N$_4$ when exposed to erosion by alumina particles.[1] The superior erosion resistance of these materials can be attributed to a combination of their high hardness, toughness and strength.

Recent studies at Monash University have established that elongated α-sialon grains can be formed *in situ* in Ca stabilized α-sialons via pressureless sintering.[5–7] In situ toughened α-sialon ceramics with an elongated morphology exhibited toughness and strength comparable to those of β-sialon while retaining the high hardness of α-sialon.[8] This indicates a great potential to produce a better sialon material for erosion resistant applications. However, elongated α-sialon grains have been observed in a number of Ca α-sialon compositions which contain various amounts of secondary phases and intergranular glass.[6,7,9] In order to optimize the erosion resistance of these materials, a better understanding of the influence of microstructural aspects including grain morphology and the presence of intergranular phases on the erosive wear mechanism is essential.

In this study, three Ca α-sialon ceramics with different grain sizes, morphologies and various amounts of intergranular glass were subjected to erosion tests. The effects of the microstructural variables on the erosion behaviour of these materials were studied. In order to clarify the influence of intergranular glassy phase on the material removal mechanisms, erosion tests were also carried out on the samples in which the intergranular glass was devitrified through a post-sintering heat treatment.

* Corresponding author. Tel.: +61-3-9905-5345; fax: +61-3-9905-4940.
E-mail address: yu.zhang@eng.monash.edu.au (Y. Zhang).

2. Experiments

2.1. Materials

Ca α-sialon can be described by the formula $Ca_{m/2}Si_{12-(m+n)}Al_{(m+n)}O_nN_{16-n}$ and has a phase region which extends two-dimensionally on the Si_3N_4-3/2(Ca_3N_2)·3AlN-4/3(AlN·Al_2O_3) plane of the Jänecke prism.[9,10] The *m* and *n* are substitution numbers referring to *m*(Al–N) and *n*(Al–O) bonds replacing (*m*+*n*)(Si–N) bonds in each unit cell.[11] The three α-sialon compositions selected for this study lie nominally along a line with *m*:*n*=2:1 on the plane mentioned above (Fig. 1). The designation CA1005 refers to a design composition of *m*=1.0 and *n*=0.5 in the α-sialon formula, and CA2613 and CA3618 describe the material of compositions *m*=2.6, *n*=1.3 and *m*=3.6, *n*=1.8, respectively. The starting powders used were Si_3N_4 (H.C. Starck, Grade M11; oxygen content 1.2 wt%), AlN (H.C. Starck, Grade AT; oxygen content 1.14 wt%) and $CaCO_3$ (APS Chemicals, Australia, Laboratory Grade). Compositional correction was made to account for the oxygen content in nitride powders. The powder mixture was ball milled in isopropanol for 30 h using Si_3N_4 media. After drying, the powders were uniaxially pressed into 25 mm diameter pellets, followed by cold isostatic pressing at 200 MPa. The pellets were packed in a 50 wt% Si_3N_4:50 wt% BN powder bed inside a graphite die and were calcined at 900°C for 1 h in vacuum to decompose $CaCO_3$ to CaO. Sintering was carried out at 1800°C for 4 h in a graphite furnace in a nitrogen atmosphere. The furnace heating rate was 20 °C min⁻¹. Cooling took place in the furnace by switching off the power after the scheduled dwell. The cooling rate was

estimated to be approximately 40°C min⁻¹ from 1800 to 1500°C and 25°C min⁻¹ between 1500 and 1200°C. Post-sintering heat treatment was carried out at 1300°C for 12 h in nitrogen since previous studies have indicated that such heat treatment results in the crystallization of the intergranular glassy phase in Ca α-sialon materials.[5,12]

2.2. Characterization

The bulk density of the target sialon ceramics was determined using the boiling water method.[13] The bulk density of hot-pressed samples of similar composition, reported in the literature, was used as a reference for the true density of the target materials.[14] The total porosity, *P*%, of the target materials was calculated from $P\% = (d_t - d_b)/d_b \cdot 100$, where d_t and d_b are the true density and bulk density of the target materials.[15]

The hardness and fracture toughness of the sialon ceramics were measured using the Vickers indentation method at a load of 98 N.[16] A value of 240 GPa for Young's Modulus was used to evaluate the fracture toughness of the Ca α-sialon materials.[17]

The phases present in the Ca α-sialon ceramics were identified using X-ray diffraction (XRD) analysis, carried out on a Rigaku-Geigerflex diffractometer with nickel filtered CuK_α radiation. Microstructures of the polished and etched samples were examined using a Jeol FE6300 scanning electron microscope (SEM) equipped with a field emission gun. Etching was performed by immersing polished surfaces of the samples into molten NaOH (~400°C) for 10 s. Prior to SEM examination, the samples were carbon coated to prevent charge accumulation. The accelerating voltage used was 10 kV. The eroded surfaces were ultrasonically cleaned in methanol, dried, sputter coated with carbon and examined using SEM.

The diameter and length of α-sialon grains were determined as the lengths of the shortest and the longest diagonal of the two-dimensional exposed grains, respectively, from the SEM micrographs of polished surfaces. Over 500 grains of each sample were measured. The apparent aspect ratio of the grains was given by the ratio of the average length over average diameter. No stereological factors were considered here.

2.3. Erosion tests

The erosion tests were carried out using commercial grade SiC abrasive grits (Norton Black). The grits were angular in shape and ranged in size between 210 and 500 μm (Fig. 2). The particle size distribution analysis, as determined by the laser diffraction technique, showed the median diameter to be $d_{50} = 388$ μm. The apparent solid density of the erodent particles was determined using a helium pycnometer. Hardness and indentation
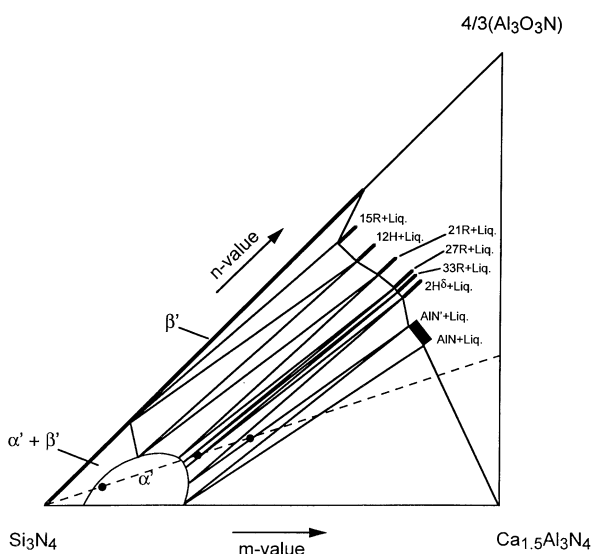
Fig. 1. Ca α-sialon phase diagram published by Hewett et al.[10] and later Wood et al.[9] The dashed line presents the compositions with an *m*:*n*=2:1 ratio and the three dots on the line indicate the three compositions chosen for the present work.

fracture toughness of the erodent particles were determined by micro-indentation tests at a load of 1.96 N. The erodent particles were mounted in thermosetting resin, ground and polished to 0.5 μm diamond finish prior to the indentation test.

Erosion tests were performed in a gas-blast type erosion test rig which has already been described in detail previously.[18] Mild steel was employed as the control material in each test. The test conditions were as follows: the sample-nozzle stand off distance was 13.8 mm; the particle velocity 20 m/s and the impact angle 90°. Each sample was eroded with a fixed amount of erodent for nine exposures. The dosage used was approximately 106 g. Mass loss from the target materials was measured using an analytical balance with an accuracy of ±0.1 mg. Wear volume was calculated from the mass loss and the bulk density of each material. Cumulative volume loss was plotted as a function of the amount of erodent impacting on the surface. The steady state erosion rate (ΔE), defined as the volume loss from the specimen per unit mass of erodent used, was determined from the slope of the linear part of the volume loss-mass of erodent plot.

3. Results

3.1. Microstructure

The crystalline phases in materials CA1005, CA2613 and CA3618 before and after heat treatment are shown in Table 1. Ca α-sialon was the dominant phase in all samples.

In material CA1005, α-sialon was the only phase revealed. In material CA2613, α-sialon was the dominant phase but there was also a trace of $2H^\delta$ (AlN-polytypoid). In material CA3618, α-sialon was again the dominant phase but small amounts of $2H^\delta$ and AlN′ were also present. It has been established that AlN-polytypoid

phases, in this case the $2H^\delta$ phase, are AlN defect structures that result from the incorporation of silicon and oxygen atoms into the AlN structure.[9,19] The AlN′ phase had a very similar XRD spectrum to the AlN starting powder. However, another study suggested that the AlN′ phase is not unreacted AlN powder, but rather a precipitated silicon-containing AlN solid solution.[6]

Table 1 also shows that there is a slight decrease in the amount of α-sialon with the increase in the *m*-value of the compositions. This decrease was accompanied by the presence of a small amount of $2H^\delta$ phase in sample CA2613, and $2H^\delta$ and AlN′ phases in sample CA3618. Furthermore, in the heat-treated CA1005, no gehlenite phase ($Ca_2Al_2SiO_7$) was found. However, in the heat-treated CA2613 and CA3618, a minor gehlenite phase existed. Gehlenite is the crystallised form of the intergranular glass and the very low content of this phase in CA1005, being at most less than 3%, indicates a very low amount of glass in the sample. The result is consistent with the fact that the CA1005 composition is located inside the single α-sialon phase region. It is important to note that the relative XRD peak intensity ratio between gehlenite $I_{(211)}$ and Ca α-sialon $I_{(102)}$ is 0.13 for sample CA2613 and 0.34 for CA3618. This suggests that the amount of intergranular glass increased with the increase in the *m*-value of the composition.

SEM micrographs of polished and chemically etched surfaces of the three Ca α-sialon ceramics are shown in Fig. 3. The average diameter, length and apparent aspect ratio of α-sialon grains of these materials are given in Table 2.

Sample CA1005 contained almost equiaxed α-sialon grains with a large fraction of the grains being slightly elongated with an aspect ratio less than 2 [Fig. 3(a)]. The size of the α-sialon grains varied widely from 0.1 to over 2 μm with an average diameter of 0.44 μm.

Sample CA2613, as shown in Fig. 3(b), displayed two distinct crystalline phases: the α-sialon phase with a smooth trait and the AlN-polytypoid phase with speckled
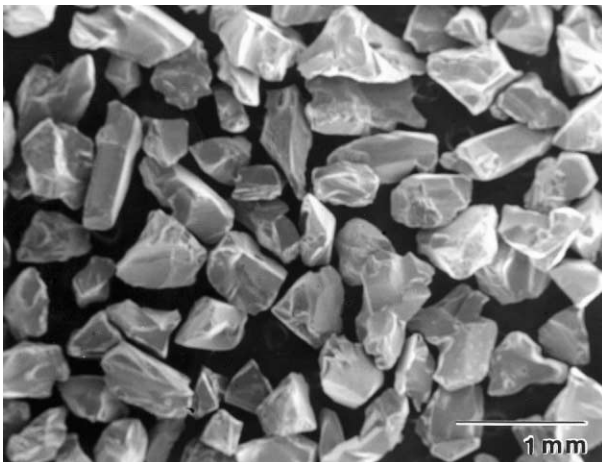

Fig. 2. SEM micrograph of as-received SiC erodent particles.

Table 1
Crystalline phases of Ca α-sialon samples prior to and post heat treatment[a]

Sample[b]	*m*-Value	α′[c]	$2H^{\delta c}$	AlN′[c]	G[c]
CA1005(AS)	1.0	vs	-	-	-
CA1005(HT)	1.0	vs	-	-	-
CA2613(AS)	2.6	vs	vw	-	-
CA2613(HT)	2.6	vs	vw	-	w
CA3618(AS)	3.6	vs	w	w	-
CA3618(HT)	3.6	vs	w	w	mw

[a] α′ = α-sialon; $2H^\delta = Si_{2.4}Al_{8.6}O_{0.6}N_{11.4}$ (AlN-polytypoid); AlN′ = aluminium nitride solid solution; G = gehlenite ($Ca_2Al_2SiO_7$) or more likely gehlenite solid solution ($Ca_2Al_{2-x}Si_{1+x}O_{7-x}N_x$[39]).

[b] AS: as-sintered; HT: heat-treated at 1300°C for 12 h in N_2.

[c] X-ray peak intensities: vs = very strong (relative peak intensity >85%), mw = medium weak (20–40), w = weak (10–20), vw = very weak (<10).

Table 2
Average diameter, length and apparent aspect ratio of α-sialon grains for the three Ca α-sialon ceramics

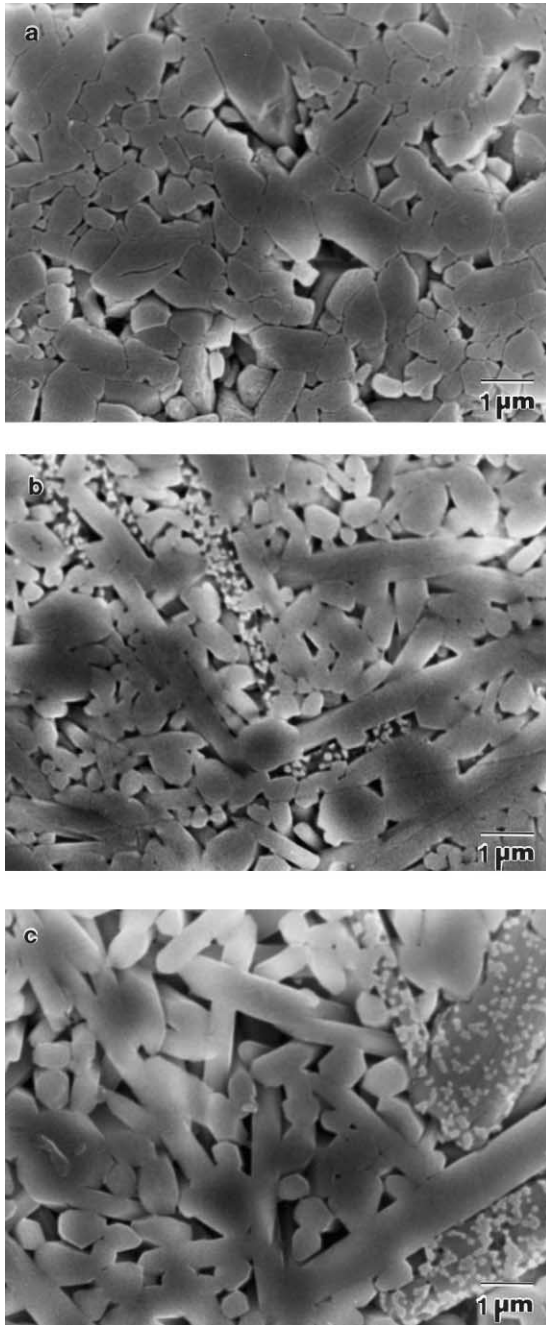| Material	Average diameter (μm)	Average length (μm)	Apparent aspect ratio
CA1005	0.44	0.69	1.6
CA2613	0.46	2.38	5.2
CA3618	0.57	4.18	7.3

Fig. 3. SEM micrographs of Ca α-sialon samples: (a) CA1005, (b) CA2613 and (c) CA3618. The samples were polished and chemically etched in molten NaOH for 10 s prior to SEM examination.

features. The α-sialon grains appeared mainly in an elongated shape and ranged widely in size. The small grains were typically 0.2–0.3 μm in diameter and 0.7–1.2 μm in length, while the large grains were 0.9–1.2 μm in diameter and 3–8 μm in length. Their aspect ratios were, however, very similar, ranging from 3 to 8 with an apparent ratio of 5.2. 2H$^\delta$ AlN-polytypoids appeared as long laths with an average thickness and length of 0.6 and 4 μm, respectively. The speckled appearance of 2H$^\delta$ grains was the result of the faster etching rate of AlN compared to that of α-sialon when NaOH etchant was used.[20]

Sample CA3618, according to XRD analysis (Table 1), consisted of three crystalline phases: the α-sialon, 2H$^\delta$ and AlN′ phases. However, only two of these phases, namely the α-sialon and 2H$^\delta$ phases, could be identified from the SEM micrograph [Fig. 3(c)]. The AlN′ phase was shown from previous work to have an equiaxed or globular morphology.[6,9] Therefore, it is difficult to distinguish the AlN′ phase from α-sialon phase on the basis of SEM examinations of polished sections. The α-sialon phase in CA3618 had a similar elongated grain morphology to that observed in material CA2613 except that it was much larger and longer in size. The average diameter for α-sialon grains was 0.57 μm, although some grains were as large as 2 μm in diameter. The apparent aspect ratio was 7.3. The 2H$^\delta$ laths in CA3618 also exhibited much larger dimensions compared to those in sample CA2613. The substantial grain growth of α-sialon and 2H$^\delta$ was due to an increased amount of glass in material CA3618.

SEM microstructural observations agree well with the XRD results: as the m-value increases, Ca α-sialon compositions exhibit lower α-sialon and higher glass and AlN' contents. The size and aspect ratio of the α-sialon grains are also found to increase with the m-value.

3.2. Physical properties

The physical and mechanical properties of the target materials are presented in Table 3, where some interesting trends can be observed. Compositions with higher m-values are easier to densify than those with lower m-values. The increase in the amount of intergranular glassy phase with increase in the m-value may account for this. Material CA3618 attained a bulk density of above 99.7% of its true density whereas material CA1005 only achieved a bulk density of 95.5% of its true density. Clearly, intergranular glassy phase or the liquid phase when it is above the eutectic temperature is crucial for facilitating densification during sintering. Further, the post-sintering heat treatment resulted in a slight decrease in the bulk density of the samples. This may be accounted for by an increased porosity resulting from the volume reduction due to the devitrification of the intergranular glass.[21] The increase in porosity at

grain boundaries was indeed observed in a recent study on grain boundary devitrification of Sm α-sialon ceramics.[22]

In Table 3, it is also seen that the hardness of the materials decreases with increasing m-value. As the m-value increases, the amount of α-sialon decreases and that of the glass increases. Thus CA1005 has the highest hardness, with values of 16.4 and 15.5 GPa for the as-sintered and heat-treated samples, respectively. CA3618 exhibits the lowest hardness, with corresponding values of 14.5 and 14.1 GPa, respectively. A slight reduction in

hardness was noticed for the heat-treated samples compared to the as-sintered ones. This may also be accounted for by the increased porosity resulting from glass devitrification in the heat-treated samples.

Indentation fracture toughness measurements of the three α-sialon compositions indicate that toughness increases with increasing m-value. The improved toughness in samples with higher m-values can be attributed to the presence of the elongated α-sialon grains as well as the large polytypoid laths in these materials. This can be evidenced by earlier studies on the fracture surfaces of high m-value materials dominated by elongated α-sialon grains in which microstructural toughening mechanisms such as grain debonding and grain pullout were observed.[7]

3.3. Erosion behaviour

Fig. 4 presents the cumulative volume loss due to erosion of the Ca α-sialon ceramics as a function of the amount of SiC erodent impinging on the material surface. In all cases, cumulative volume loss increases linearly with the amount of erodent after an incubation period. The slope of this linear portion was used to obtain the steady-state erosion rate. This linear relationship between the volume loss and the amount of the
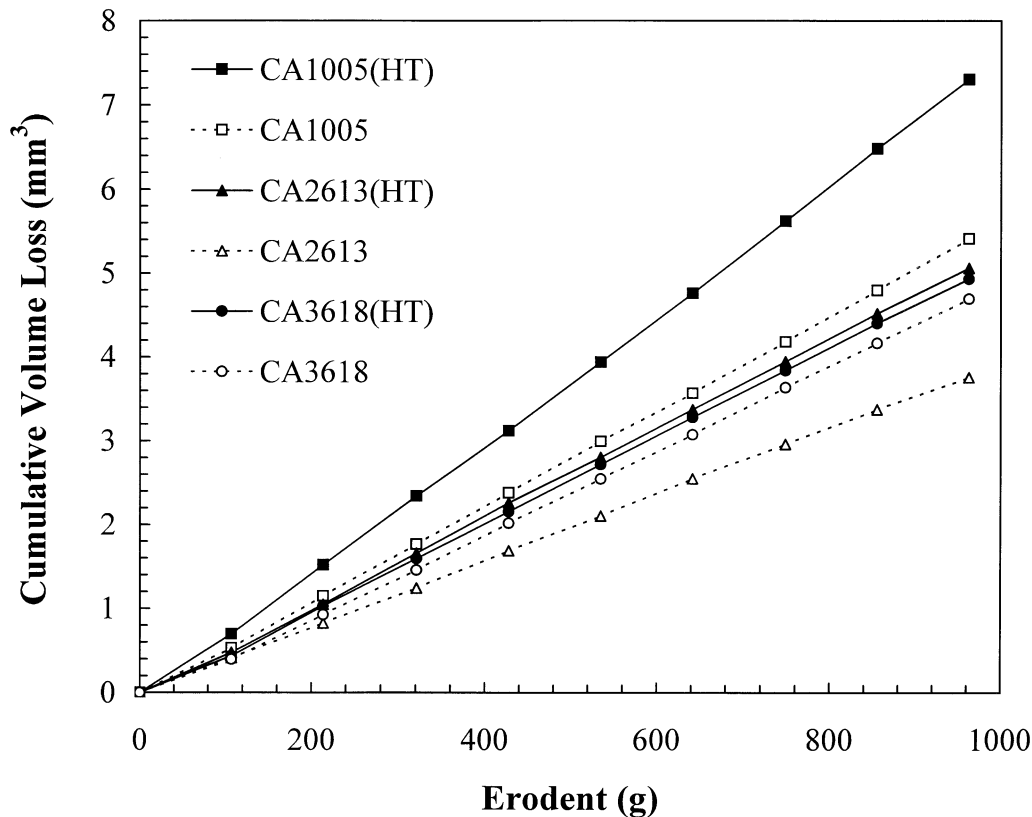
Table 3
Properties of the erodent and target materials

Sample	Bulk density (kg/m^3)	True density[a] (kg/m^3)	Total porosity (%)	Hardness (GPa)	Toughness (MPa m$^{1/2}$)
SiC erodent	–	3208	–	31.7±0.2[b]	2.4±0.1[b]
CA1005(AS)	3035	3170	~4.45	16.4±0.3	4.5±0.1
CA1005(HT)	3033	–	~4.52	15.5±0.3	4.6±0.4
CA2613(AS)	3150	3210	~1.90	15.0±0.3	5.4±0.5
CA2613(HT)	3150	–	~1.90	14.7±0.2	5.5±0.1
CA3618(AS)	3205	3210	~0.16	14.5±0.3	5.7±0.3
CA3618(HT)	3200	–	~0.31	14.1±0.4	5.9±0.2

[a] Bulk density of hot-pressed samples.
[b] Measured by Vickers indentation at 1.96 N load.

Fig. 4. Cumulative volume loss of Ca α-sialon ceramics as a function of the amount of SiC erodent impinging on the target surface. The solid symbols represent the heat-treated samples: CA1005 (■), CA2613 (▲) and CA3618 (●), while the corresponding open symbols present their as-sintered counterparts, respectively. The solid and the dashed lines are the point to point joins of data points.

erodent indicates that each consecutive dosage has removed approximately the same amount of material from the target surface.

Fig. 5 shows the steady-state erosion rates of α-sialon ceramics eroded by airborne SiC particles. As can be seen, among the three as-sintered samples, material CA1005 shows the highest rate of erosive loss and material CA2613 the lowest. This trend in erosion rates is, however, altered in their heat-treated counterparts where the erosion rate tends to decrease with the increasing m-value, although the erosion rates of the heat-treated CA2613 and CA3618 appear to be very similar. In all cases, the heat-treated samples display a higher erosion rate than their as-sintered counterparts and the difference in erosion rate between the heat-treated and the as-sintered samples decreases with the increasing m-value.

3.4. SEM observations

The erosion craters formed by airborne SiC erosion at normal impact are circular in shape. To facilitate comparison of damage sustained by individual samples, the SEM micrographs were taken at or near the centre of the erosion crater.

Fig. 6(a) shows a general view of the eroded surface of as-sintered sample CA2613, while Fig. 6(b) shows the centre-right region of Fig. 6(a) at a higher magnification.

Similarly, Fig. 6(c) presents the general view of the eroded surface of the heat-treated sample CA2613 and Fig. 6(d) is a higher magnification micrograph of the centre-left region of Fig. 6(c). It can be seen that the morphology of the eroded surface is quite different for the as-sintered and heat-treated samples. For as-sintered material CA2613 [Fig. 6(a)], the damaged surface appears to be relatively smooth and contains some small-scale faceted regions. The higher magnification micrograph [Fig. 6(b)] reveals that the damage features for the as-sintered sample were mainly transgranular fracture and smearing of the deformed materials. Transgranular fracture was even observed in the elongated grains which were oriented virtually parallel to the target surface, as marked by arrows in [Fig. 6(b)], indicating that the intergranular calcium oxynitride glass provided a strong bonding between the grains. Further, in many cases, the skeletons of the underlying grains were observed in the plastically deformed regions, indicating the preferential removal of the softer glassy phase. In contrast, for the heat-treated material CA2613 [Fig. 6(c)], the erosion damage is clearly more severe. Higher magnification SEM examination [Fig. 6(d)] showed that erosion damage involved both transgranular and intergranular fractures, as well as localized plastic deformation. Intergranular fracture, evidenced as grain pull-outs, is caused by substantial grain boundary microcracking and was often observed for
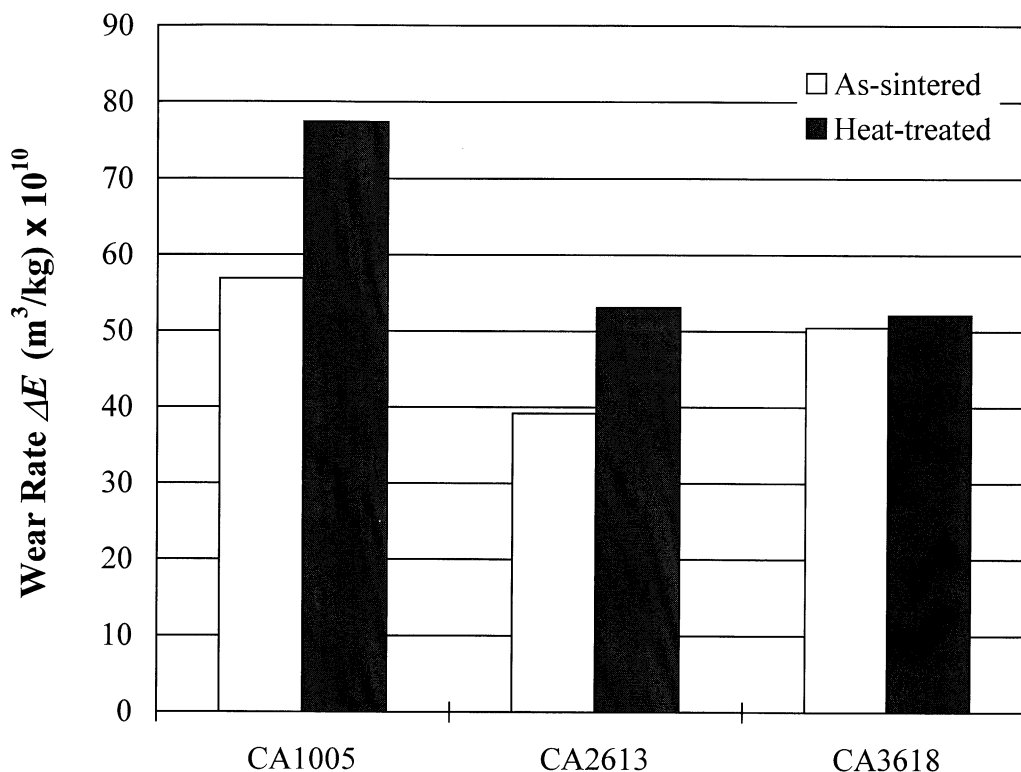

Fig. 5. Steady-state erosion rates of α-sialon ceramics eroded by airborne SiC particles after 90° impingement. Shaded bars represent the erosion rates of the heat-treated samples, while clear bars show the erosion rates of the as-sintered samples.
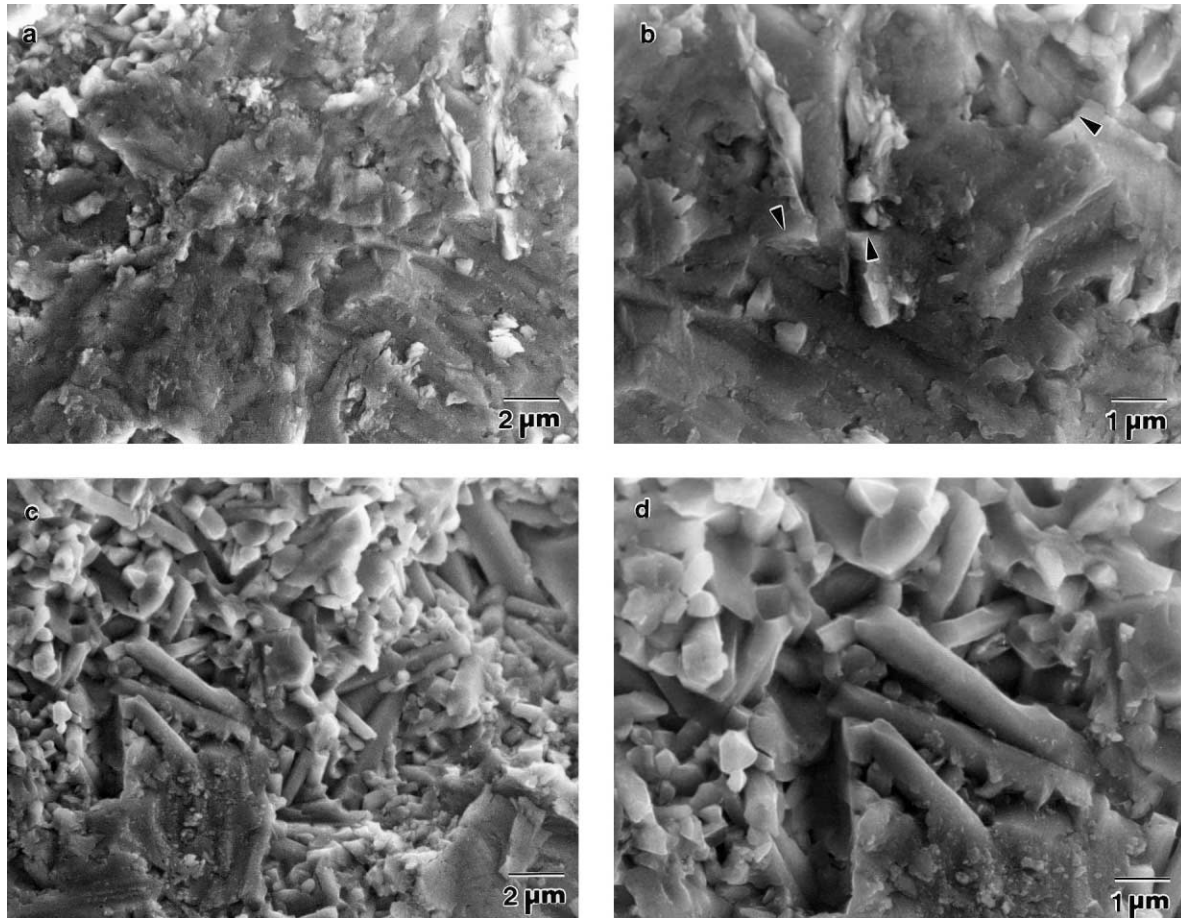
Fig. 6. SEM micrographs of steady-state erosion surfaces of material CA2613 after 90 °impingement: (a) and (b), as-sintered sample; (c) and (d), heat-treated sample. Note: arrows in (b) indicate the transgranular fracture of the elongated grains which are oriented virtually parallel to the eroding surface.

equiaxed grains as well as some elongated grains that were oriented parallel to the surface.

When as-sintered material CA3618 was exposed to SiC erosion at normal impact, as shown in [Fig. 7(a)], the damage patterns were again dominated by transgranular fracture and plastically deformed materials. On the other hand, when the heat-treated CA3618 sample was eroded by SiC particles, as shown in [Fig. 7(b)], profuse grain boundary microcracking occurred. The higher magnification SEM examination [Fig. 7(c)] showed that the main material removal mechanisms were transgranular fracture and grain dislodgment.

The eroded surfaces of material CA1005, both as-sintered and heat-treated, are presented in Fig. 8(a) and (b), respectively. As can be seen, in both cases, the damage features were governed by grain ejection and plastically deformed materials coupled with small-scale chipping. This is, however, quite different from the damage features observed in as-sintered materials CA2613 and CA3618 where transgranular fracture was the dominant material removal mechanism.

4. Discussion

When brittle materials are exposed to impact by hard and sharp particles, the resulting damage patterns show some degree of similarity to those produced by a sharp indenter such as a Vickers diamond pyramid indenter. Accordingly, the more controlled indentation process has been used to model the dynamic erosion process.[23–25] Two theoretical models, the dynamic and the quasi-static models, have been developed to describe the elastic–plastic damage caused by sharp particle contact.[23,24] Both these models predict the erosion rate as:

$$\Delta E \propto v^n D^{3.7} \rho^p K_c^{-1.3} H^q \tag{1}$$

where ΔE is the erosion rate; v, D and ρ are the velocity, mean diameter and density of the erodent particles; and K_c and H are the fracture toughness and hardness of the target material. The exponents n, p and q differ in the two models, being 3.2, 1.3 and −0.25 for the dynamic model and 2.4, 1.2 and 0.11 for the quasi-static model,

Fig. 8. SEM micrographs of steady-state erosion surfaces of sample CA1005 after 90° impingement: (a) as-sintered sample and (b) heat-treated sample.
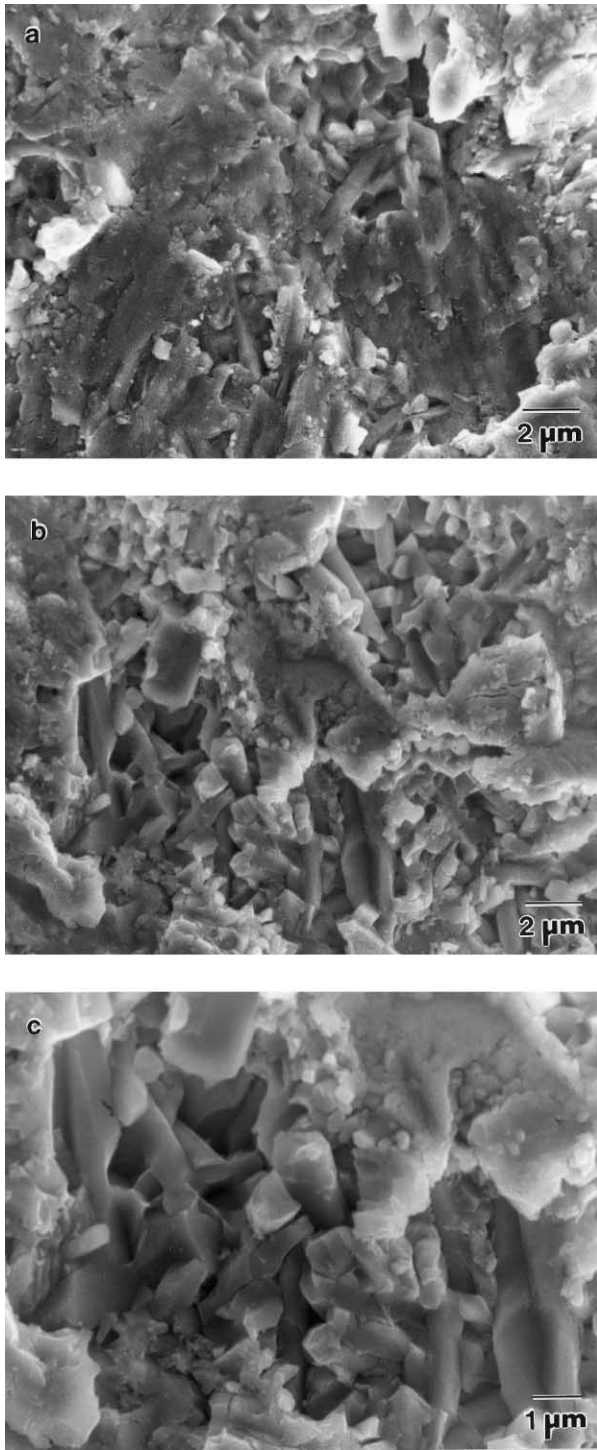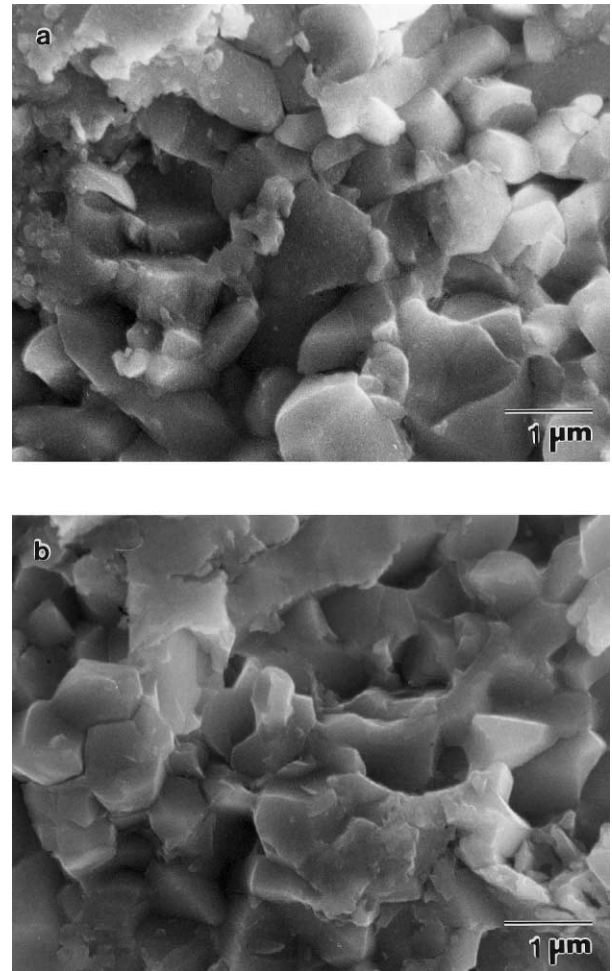

Fig. 7. SEM micrographs of steady-state erosion surfaces of material CA3618 after 90° impingement: (a) as-sintered sample; (b) and (c) heat-treated sample.

respectively. As can be seen, both models suggest that the erosion rate has a strong inverse dependence on the fracture toughness, but has a much weaker dependence on the hardness of the target material.

The validity of these two models has been tested on a wide range of ceramic materials.[1,26–28] The results,

however, vary from one system to another. For example, for erosion of alumina ceramics, it was well established that the erosion rate does not simply depend on the hardness and fracture toughness of the target materials. In fact, the microstructure of the target materials has been shown to have a controlling effect on the material removal mechanism.[18,29–31] On the other hand, for erosion of sialon ceramics, the only two published systematic studies showed a qualitative agreement between the experimental results and the two theoretical models: the erosion rate decreases strongly with the increasing fracture toughness, but less sensitively with the increasing hardness.[1,2] However, such qualitative agreements are not supported by this work. While the most erosion resistant Ca α-sialon composition, CA2613, possesses moderate hardness and toughness values, the other two compositions have either higher hardness (CA1005) or higher toughness (CA3618) than CA2613. Nevertheless, both are less erosion resistant than sample CA2613. The discrepancies between our observation and the two theoretical models may be

explained in terms of the microstructural characteristics of the target materials.

The major microstructural parameters for ceramic materials are porosity, crystalline phases, grain size and morphology and the nature of the grain boundary phases. It is the primary interest of the present study to examine the effects of these microstructural parameters on the erosion behaviour of α-sialon ceramics.

The dominant material removal mechanism for the as-sintered CA2613 and CA3618 samples is transgranular fracture [Figs. 6(a) and 7(a)], but for CA1005 is intergranular fracture [Fig. 8(a)]. Both CA2613 and CA3618 consist mainly of randomly oriented elongated α-sialon grains and large $2H^{\delta}$ laths. The interlock effect of the elongated grains effectively hindered the grain dislodgment mechanism. Thus, more energy is required to remove the interlocked elongated grains from the target surface than to dislodge equiaxed grains. The interlock effect hypothesis is further supported by our SEM observations of the eroded surfaces of the heat-treated materials CA2613 and CA3618. As shown in Figs. 6(d) and 7(c), despite the substantial intergranular cracking, the transgranular fracture of the interlocked long α-sialon grains still remains as one of the dominant material removal mechanisms.

The major microstructural difference between the two high *m*-value compositions is that CA2613 possesses a fine elongated grain morphology with relatively less grain boundary glass and higher porosity while CA3618 exhibits a coarser and longer grain morphology coupled with a higher amount of grain boundary glass and an additional minor AlN′ phase.

It is well known that porosity has a deleterious effect on erosion resistance because the pores, especially those at grain boundary triple junctions, can be regarded as a stress-concentrating flaw system[32] and consequently become preferred sites for microcrack initiation.[33] Thus, from the porosity point of view, the more porous material CA2613 should have inferior erosion resistance than CA3618. However, our experiments revealed a lower erosion rate for CA2613 compared to CA3618 (Fig. 5).

The crystalline phases and the grain size can influence the erosion behaviour of the ceramic materials. However, our erosion tests showed the heat-treated samples CA2613 and CA3618 displayed a comparable erosion rate (Fig. 5), suggesting that for sialon compositions with a similar grain morphology, minor differences in crystalline phases, grain sizes and the amount of crystallized intergranular phases do not significantly influence the erosion resistance.

It can, therefore, be concluded that the excessive amount of intergranular glass in sample CA3618 is primarily responsible for its poorer erosion performance, as the glassy phase is, in general, much less resistant to erosion than the α-sialon grains. On the other hand, an optimum amount of grain boundary glass may improve the erosion resistance of these ceramics. Grain boundary glass fills into the pores and facilitates the particle rearrangement during the sintering and also has the potential to absorb or cushion the stress induced from solid particle impact via viscous flow.

The Ca oxynitride glass present in the Ca α-sialon ceramics has a relatively low T_g point (800–900°C).[34] Thus, the glass in the vicinity of the impact site could be softened due to local adiabatic heating caused by the impact of the fast-moving particles.[18,35,36] In a previous study of erosion of these materials by garnet particles under similar conditions, it was observed that the local adiabatic heating effect resulted in the melting of the erodent particles whose melting point is 1250°C.[37] Moreover, if the grain boundary glass has strong bonding with the elongated ceramic grains, it would make intergranular fracture and grain ejection more difficult upon erosion. This effect could be especially significant in α-sialon ceramics because in α-sialon, unlike in β-sialon and $\beta\text{-}Si_3N_4$, both grain boundary glass and α-sialon grains contain identical elements. Thus, the bonding between α-sialon grains and the glassy matrix could be strong. The contribution of intergranular phases to the erosion process can be further illustrated by comparing the α-sialon samples before and after post-sintering heat treatment.

The erosion test results showed that the as-sintered material CA2613 possessed significantly higher erosion resistance than its heat-treated counterpart (Fig. 5). The post-sintering heat treatment can have three effects on α-sialon materials: (1) the partial crystallization of the excess glass located at three-grain edges,[38] which can result in up to 10% volume reduction in the Ca α-sialon system[12] and thus produces a radial tensile stress in the triple junctions at the interface between the α-sialon grains and the gehlenite phase;[38] (2) the formation of the gehlenite phase which leads to an enrichment of the nitrogen content in the grain boundary glass film and the residual glass at the three-grain edges; and (3) the creation of thermal stresses at the three-grain edges due to thermal expansion mismatch between the α-sialon grains and devitrified phases.

The volume reduction and the creation of thermal stresses can generate microcracks or even pores at the grain boundary triple junctions and consequently weaken the bonding strength between the α-sialon grains and the gehlenite phase. The weakened grain boundary triple junctions can be regarded as preferred sites for microcrack initiation upon erosion and thus degrade the erosion resistance of the α-sialon ceramics.

The gehlenite phase observed in the Ca α-sialon system is a member of the melilite group and can also exist as a solid solution incorporating a small amount of nitrogen with the general formula $Ca_2Al_{2-x}Si_{1+x}O_{7-x}N_x$.[39] However, the formation of the gehlenite solid solution consumes much more oxygen than nitrogen

and hence results in a residual glass with increased nitrogen content and increased viscosity. This is because in glass structure, nitrogen possesses three bonds which increase the packing density and the stiffness of the network.[40] The higher viscosity residual glass can further degrade the erosion resistance of the α-sialon ceramics because of the reduction in the ability of grain boundary to viscoplastically absorb or cushion the impact stress.[41] This scenario is supported by the SEM study on the eroded surfaces of material CA2613. As shown in Fig. 6(b), the material removal mechanism for the as-sintered sample is predominantly transgranular fracture, indicating strong bonding between the grains. In contrast, the eroded surface of heat-treated sample CA2613 [Fig. 6(d)] revealed substantial grain boundary microcracking and grain dislodgment.

Comments may be made on erosion behaviour of material CA1005. It has been shown that the dominant material removal mechanism, for both as-sintered and heat-treated samples, was grain ejection coupled with small-scale chipping. This is because material CA1005 contains approximately equiaxed grains and a very small amount of intergranular glass, which is mainly responsible for a relatively large number of pores in the sample. The linkage of the pre-existing flaws and the substantial grain boundary microcracks induced from the severe impacts results in the ejection of the equiaxed grains. Thus, material CA1005 has the highest erosion rate of the three compositions. Furthermore, small-scale chipping is evidence of the severity of the damage produced by SiC erosion owing to its extremely high hardness. Finally, heat treatment has further weakened the intergranular bonding strength of the material, resulting in poor performance in the erosion tests (Fig. 5).

5. Conclusions

The present study has clearly demonstrated that microstructural parameters such as grain size, grain morphology, and the amount of intergranular glass can all play a role in determining the erosion behaviour of Ca α-sialon ceramics. The following conclusions can be made from the results of this study.

- For material consisting of fine approximately equiaxed grains (CA1005), the dominant material removal mechanism is grain ejection, while for materials containing mostly elongated grains (CA2613 and CA3618), it is transgranular fracture. This is because the interlock effect of the elongated grains hinders the grain ejection mechanism.
- An optimum amount of intergranular glass may improve the erosion resistance of α-sialon ceramics due to the following reasons: (1) grain boundary glass reduces the amount of porosity in the material;

(2) grain boundary glass forms strong bonds with the α-sialon grains due to the similarity in their respective chemical compositions; and (3) grain boundary glass has the potential of absorbing and cushioning the stress induced by solid particle impacts.
- An excess amount of grain boundary glass will result in poorer erosion performance due to the lower erosion resistance of the glass phase compared to α-sialon.
- Post-sintering heat treatment increases the erosion rate of Ca α-sialon materials. Such differences can be attributed to (1) the weakening of the bond strength between the α-sialon grains at the three-grain edges due to the volume reduction induced from the devitrification of the intergranular glass; (2) the creation of the intergranular stresses due to thermal expansion mismatch between the α-sialon grains and devitrified phases; and (3) the reduction of the ability of the grain boundary to viscoplastically absorb or cushion the stresses during erosion owing to the crystallization of the intergranular glass.

References

1. Wada, S., Effect of hardness and fracture toughness of target materials and impact particles on erosion of ceramic materials. In *Erosion of Ceramic Materials*, ed. J. E. Ritter. Trans. Tech. Publications, Switzerland, 1992, pp. 51–74.
2. Liu, D.-M., Lin, J.-T. and Lee, R. R.-R., Erosive wear behaviour in duophase sialon composites. *Ceram. Int.*, 1998, **24**, 217–221.
3. Hewett, C. L., Cheng, Y.-B., Muddle, B. C. and Trigg, M. B., Preparation of fine-grained calcium α-sialon. *J. Mater. Sci. Lett.*, 1994, **13**, 1612–1615.
4. Ekström, T. and Nygren, M., Sialon ceramics. *J. Am. Ceram. Soc.*, 1992, **75**(2), 259–276.
5. Hewett, C. L., *The fabrication and characterisation of Ca α-sialon ceramics*. PhD thesis, Monash University, Melbourne, Australia, 1998.
6. Zhao, H., Swenser, S. P. and Cheng, Y.-B., Elongated α-sialon grains in pressureless sintered sialon ceramics. *J. Eur. Ceram. Soc.*, 1997, **18**, 1053–1057.
7. Wood, C. A., Zhao, H. and Cheng, Y.-B., Microstructural development of Ca α-sialon ceramics with elongated grains. *J. Am. Ceram. Soc.*, 1999, **82**(2), 421–428.
8. Chen, I.-W. and Rosenflanz, A., A tough SiALON ceramic based on α-Si₃N₄ with a whisker-like microstructure. *Nature*, 1997, **389**, 701–704.
9. Wood, C. A. and Cheng, Y.-B., Phase relationships and microstructures of Ca and Al-rich α-sialon ceramics. *J. Eur. Ceram. Soc.*, 2000, **20**, 357–366.

10. Hewett, C. L., Cheng, Y.-B., Muddle, B. C. and Trigg, M. B., Phase relationships and related microstructural observations in the Ca–Si–Al–O–N system. *J. Am. Ceram. Soc.*, 1998, **81**(8), 1781–1788.

11. Cao, G. Z. and Metselaar, R., α′-Sialon ceramics: a review. *Chem. Mater.*, 1991, **3**, 242–252.

12. Malecki, A., Gajerski, R., Labus, S., Prochowska-Klisch, B. and Oblakowski, J., Kinetics and mechanism of crystallization of gehlenite glass pure and doped with Co^{2+}, Eu^{3+}, Cr^{3+} and Th^{4+}. *J. Non-Cryst. Solids*, 1997, **212**, 55–58.

13. The determination of density, porosity and water absorption. *Standards Association of Australia*, 1979, 1–3, **AS 1774.5**.

14. Wang, P. L., Zhang, C., Sun, W. Y. and Yan, D. S., Characteristics of Ca-α-sialonphase formation, microstructure and mechanical properties. *J. Eur. Ceram. Soc.*, 1999, **19**, 553–560.

15. Andreola, F., Leonelli, C., Romagnoli, M. and Miselli, P., Techniques used to determine porosity. *Am. Ceram. Soc. Bull.*, 2000, **79**(7), 49–52.

16. Antis, G. R., Chantikul, P., Lawn, B. R. and Marshall, D. B., A critical evaluation of indentation techniques for measuring fracture toughness: I, Direct crack measurements. *J. Am. Ceram. Soc.*, 1981, **64**(9), 533–538.

17. Ta, W., Cheng, Y.-B., Muddle, B., Hewett, C. and Trigg, M., Pressureless sintering of calcium alpha sialons. *Mater. Sci. Forum*, 2000, **325–326**, 199–206.

18. Zhang, Y., Cheng, Y.-B. and Lathabai, S., Erosion of alumina ceramics by air- and water-suspended garnet particles. *Wear*, 2000, **240**, 40–51.

19. Van Tendeloo, G., Faber, K. T. and Thomas, G., Characterization of AlN ceramics containing long-period polytypes. *J. Mater. Sci.*, 1993, **18**, 525–532.

20. Weimer, A. W., *Carbide, Nitride and Boride Materials Synthesis and Processing*. Chapman & Hall, London, 1997, pp. 159–164.

21. Deckwerth, M. and Rüssel, C., Crystallization of oxynitride glasses in the system Mg–Ca–Al–Si–O–N prepared with the aid of a polymeric precursor. *J. Non-Cryst. Solids*, 1997, **217**, 55–65.

22. Cheng, Y.-B. and Thompson, D. P., Preparation and grain boundary devitrification of samarium α-sialon ceramics. *J. Eur. Ceram. Soc.*, 1994, **14**, 13–21.

23. Evans, A. G., Gulden, M. E. and Rosenblatt, M., Impact damage in brittle materials in the elastic-plastic response regime. *Proc. Roy. Soc. London, Ser. A*, 1978, **361**, 343–365.

24. Wiederhorn, S. M. and Lawn, B. R., Strength degradation of glass impacted with sharp particles: I, Annealed surfaces. *J. Am. Ceram. Soc.*, 1979, **62**(1-2), 66–70.

25. Rowcliffe, D. J., Quasi-static indentation of ceramics. In *Erosion of Ceramic Materials*, ed. J. E. Ritter. Trans. Tech. Publications, Switzerland, 1992, pp. 1–22.

26. Routbort, J. L., Scattergood, R. O. and Kay, E. W., Erosion of silicon single crystals. *J. Am. Ceram. Soc.*, 1980, **63**(11–12), 635–640.

27. Wiederhorn, S. M. and Hockey, B. J., Effect of material parameters on the erosion resistance of brittle materials. *J. Mater. Sci.*, 1983, **18**, 766–780.

28. Routbort, J. L. and Scattergood, R. O., Solid particle erosion of ceramics and ceramic composites. In *Erosion of Ceramic Materials*, ed. J. E. Ritter. Trans. Tech. Publications, Switzerland, 1992, pp. 766–780.

29. Lathabai, S. and Pender, D. C., Microstructural influence in slurry erosion of ceramics. *Wear*, 1995, **189**, 122–135.

30. Lathabai, S., Erosion of ceramics. *Materials Forum*, 1995, **19**, 101–116.

31. Heath, G. R., Johnson, T. D., Parry, M. T. and Wall, D. J., Solid particle erosion of alumina linings for pulverised fuel transport piping. *Br. Ceram. Trans. J.*, 1990, **89**, 17–21.

32. Miranda-Martinez, M., Davidge, R. W. and Riley, F. L., Grain size effects on the wet erosive wear of high-purity polycrystalline alumina. *Wear*, 1994, **172**, 41–48.

33. Lawn, B. R., *Fracture of Brittle Solids*. Cambridge University Press, Cambridge, UK, 1993, Chapter 9.

34. Hampshire, S., Drew, R. A. L. and Jack, K. H., Oxynitride glasses. *Phys. Chem. Glasses*, 1985, **26**(5), 182–186.

35. Yust, C. S. and Crouse, R. S., Melting at particle impact sites during erosion of ceramics. *Wear*, 1978, **51**, 193–196.

36. Lawn, B. R., Hockey, B. J. and Wiederhorn, S. M., Thermal effects in sharp-particle contact. *J. Am. Ceram. Soc.*, 1980, **63**(5–6), 356–358.

37. Zhang, Y., Cheng, Y.-B. and Lathabai, S., Erosion behaviour of advanced ceramics. *J. Aust. Ceram. Soc.*, in press.

38. Hoffmann, M. J., High-temperature properties of Yb-containing Si_3N_4. In *Tailoring of Mechanical Properties of Si_3N_4 Ceramics*, ed. M. J. Hoffmann and G. Petzow. NATO ASI Series. Series E: Applied Sciences — Vol. 276. The Netherlands, Kluwer Academic Publishers, 1994, pp. 233–244.

39. van Rutten, J. W. T., Hintzen, H. T. and Metselaar, R., Phase formation of Ca-α-sialon by reaction sintering. *J. Eur. Ceram. Soc.*, 1996, **16**, 995–999.

40. Hampshire, S., Nestor, E., Flynn, R. et al.Yttrium oxynitride glasses: properties and potential for crystallisation to glass-ceramics. *J. Eur. Ceram. Soc.*, 1994, **14**, 261–273.

41. Stough, M. A., Hellmann, J. R. and Conway, J. C., The effect of grain-boundary devitrification on the wear of glass-bonded alumina ceramics. *J. Mater. Sci.*, 1994, **29**, 3665–3672.